nature communications

Article

https://doi.org/10.1038/s41467-025-57303-w

Scalable preparation of perovskite films with homogeneous structure via immobilizing strategy for high-performance solar modules

Received: 8 August 2024

Accepted: 18 February 2025

Published online: 28 February 2025

Check for updates

Shihao Yuan[1], Daming Zheng[2], Ting Zhang[1] ✉, Yafei Wang[3], Feng Qian[1], Lei Wang[1], Xiaobo Li[1], Hualin Zheng[1], Zecheng Diao[3], Peng Zhang[4], Thierry Pauporté[2] & Shibin Li[1] ✉

Scalable fabrication of perovskite films with homogeneous structure remains a critical challenge in bridging power conversion efficiency gap between solar modules and laboratory-scale cells. To address this, we propose a slot-die coating strategy with pyrrodiazole additives in the perovskite precursor solution to simultaneously immobilize lead iodide and formamidinium iodide. This approach enhances wet film stability by suppressing colloidal aggregation, retards the crystal growth process, and ensures a consistent growth rate across the films. These effects promote the formation of large, monolithic grains, enabling large-area perovskite films with homogeneous structure, excellent uniformity, and low defect density under ambient conditions. Using this strategy, we achieved 10 cm × 10 cm inverted perovskite solar modules with a certified efficiency of 20.3%, along with good working stability and excellent application demonstration, showcasing its great potential for industrialization.

Formamidinium iodide (FAI)-based inverted perovskite solar cells (IPSCs) have achieved great advancement in developing large-area (>50 cm^2) modules with power conversion efficiencies (PCEs) over 20%[1,2], marking a significant step toward commercialization. To further advance scalable fabrication, transitioning the perovskite deposition process from a glove box to ambient air is essential[3,4], as it simplifies manufacturing and reduces costs for large-scale production. Among various techniques, slot-die coating shows great potential for upscaling due to its low material wastage, high uniformity, and compatibility with continuous industrial production[5]. However, ambient humidity during slot-die coating accelerates crystal growth and shortens the processing window[6–10], leading to small, randomly arranged grains instead of the large, monolithic grains typically formed via spin-coating in a glove box. This results in reduced film uniformity and increased defects, causing the PCE of large-area inverted perovskite solar modules (IPSMs) to lag behind their laboratory-scale counterparts[11].

The primary challenge in achieving homogeneous structure of large-sized, monolithic grains in air is extending the stability of the perovskite precursor solution to ensure full film coverage. Solvent engineering has proven effective in addressing this issue. Lewis base solvents, such as N-methyl-2-pyrrolidinone[12], diphenyl sulfoxide[13], and N, N′-dimethylpropyleneurea (DMPU)[14], interact with perovskite precursors to enhance solubility and nucleation energy, thus extending the solution stability[15]. Then, for producing large perovskite grains, slow crystal growth following fast nucleation is crucial[15–17]. Accelerating nucleation can be achieved by promoting the rapid supersaturation of perovskite wet films, with techniques such as anti-solvent treatment[18], gas-assisted deposition[19], and vacuum flash-assisted solution process (VASP)[20] effectively removing solvents. To retard crystal growth, forming Lewis acid-base adducts using monodentate or bidentate ligands containing oxygen[21,22], sulphur[23], and nitrogen[24] atoms as coordinating sites has proven effective, primarily by forming complexes or interphases with lead iodide (PbI_2).

[1]State Key Laboratory of Electronic Thin Films and Integrated Devices, and School of Optoelectronic Science and Engineering, University of Electronic Science and Technology of China (UESTC), Chengdu, Sichuan, China. [2]Chimie ParisTech, PSL Research University, CNRS, Institut de Recherche de Chimie Paris (IRCP), UMR8247, Paris, France. [3]School of Mechanical and Electrical Engineering, Guangzhou University, Guangzhou, China. [4]College of Optical and Electronic Technology, China Jiliang University, Hangzhou, China. ✉e-mail: tzhang@uestc.edu.cn; shibinli@uestc.edu.cn

Additionally, the formation of a homogeneous structure is closely related to the grain arrangement of perovskites. Recent studies have demonstrated that the grain arrangement within perovskite film is significantly influenced by the crystallization rates at the upper and lower layers of wet films[25,26]. When these rates are similar, larger, more uniform, and monolithic grains are formed[25]. Zheng et al. further demonstrated the significance of monitoring these rates using real-time glow discharge-optical emission spectroscopy (GD-OES), a technique valuable for studying grain arrangement in large-area perovskite films[26].

Building on the discussion of nucleation, crystal growth, and the role of solvents and additives in retarding crystallization to promote larger grains, controlling the crystallization rates in the upper and lower layers of perovskite wet films is equally critical, as it directly affects grain growth and arrangement. However, changes in solvents or additives also affect the size and distribution of perovskite colloidal clusters, which subsequently influence the films' morphology and optoelectronic properties[27]. For example, agglomeration and uneven size distribution of colloidal clusters can disrupt phase uniformity and grain stacking, hindering the formation of homogeneous structured films[28]. Therefore, a comprehensive understanding of how solvents and additives impact both crystallization dynamics and colloidal size distribution is essential. By optimizing these parameters, the uniformity and scalability of large-area perovskite films can be significantly improved.

Inspired by this, we develop a simultaneous FAI and PbI_2 immobilization strategy using a pyrrodiazole (PZ) additive during the slot-die coating to achieve the scalable fabrication of high-quality perovskite films with homogeneous structure under ambient conditions. The immobilization effect, driven by the formation of Lewis acid-base pairs (PZ-PbI_2) and hydrogen bonds (PZ-FAI), not only improves the colloidal size distribution uniformity in the perovskite precursor solution but also enhances the stability of the wet film by inhibiting colloid agglomeration. Real-time characterizations reveal that this approach not only retards the crystal growth process but also ensures consistent crystallization rates between the upper and lower layers of the perovskite film. This facilitates the formation of large, monolithic grains with excellent uniformity. Based on this approach, the resulting IPSMs possess an impressive PCE of 21.5% (certified 20.3%), which ranks among the highest certified PCEs reported for IPSMs with an aperture area >50 cm^2 (Supplementary Table 1). Notably, encapsulated IPSMs retain 94% of their initial efficiency after continuous light aging in air for 1000 h under a relative humidity of 65%, and demonstrate a good practical application.

Results

Immobilization effect on colloidal uniformity

Commonly, the formation of a homogeneous perovskite film is closely related to the state of the perovskite precursor. In perovskite precursor solutions, perovskite components exist as colloids stabilized by an electrical double layer (EDL), formed through the attraction between negatively charged iodoplumbate ions and surrounding organic cations[29]. To address colloidal agglomeration and heterogeneity, we proposed an additive strategy to enhance EDL stability by strengthening interactions between iodoplumbate ions and organic cations. Triazole, a five-membered aromatic heterocyclic compound, was selected due to its dual functionality[30]: nitrogen atoms that donate lone pairs of electrons to interact with Pb^{2+} and an N-H group that forms hydrogen bonds with FA^+. These interactions hinder colloidal agglomeration and improve solution homogeneity.

As shown in Fig. 1a, triazole exists in three isomeric forms-1H-1, 2, 4-triazole (pyrrodiazole, PZ), 1H-1, 2, 3-triazole (PZ-I), and 2H-1, 2, 4-triazole (PZ-II), which differ in the positions of nitrogen atoms and N-H groups, affecting properties such as proton dissociation ability[30]. We systematically investigated the effects of these isomers on perovskite components and colloidal stability. To gain deeper insights, we began by simulating the interactions between the three additives and PbI_2 through electrostatic potential (ESP, Fig. 1a) analysis. The results showed that all three additives exhibit strong electron-donating ability at their nitrogen atoms (Supplementary Table 2), enabling the formation of Lewis acid-base pairs with PbI_2[31]. To validate this, liquid-state ^{1}H nuclear magnetic resonance (^{1}H NMR) titration measurements were performed[32,33]. As shown in Fig. 1b, the N-H proton peak of PZ (14.0 ppm) was sharper than those of PZ-I and PZ-II, attributed to PZ's significantly higher pK_a value (two orders of magnitude larger)[30], indicating that the N-H protons of PZ-I and PZ-II are more prone to dissociation in polar solutions. Upon introducing PbI_2, the N-H peaks of all three additives sharpened, confirming the formation of Lewis acid-base pairs between Pb^{2+} and the nitrogen atoms.

When mixed with FAI alone, the N-H peaks of the additives and FAI shifted and converged into a single peak (Fig. 1b), indicating strong hydrogen bonding interactions between the additives and FAI. This confirms that all three additives have the ability to interact with both PbI_2 and FAI individually. To more rigorously confirm whether these additives exhibit immobilization effect, we investigated their roles in the presence of PbI_2 and FAI. As shown in Fig. 1c, when PbI_2 and FAI were mixed, the N-H peak of FAI shifted to a lower chemical shift, indicating an interaction between the two components. Notably, only PZ caused the cleavage of the N-H proton peak of FAI in the presence of PbI_2, whereas PZ-I and PZ-II induced only minor shifts. This demonstrates that PZ estabilishes stronger interactions with both the perovskite components[31,34]. Furthermore, the flattened N-H peaks of PZ-I and PZ-II in the mixed solution suggest their proton dissociation behavior, which enhances solubility of the components but lacks the immobilization effect observed with PZ.

Dynamic light scattering (DLS) was used to evaluate the effects of the three additives on perovskite colloids. As shown in Fig. 1d, PZ effectively prevented the formation of large colloids (>1000 nm), ensuring that the host colloids are predominantly distributed within a uniform small-size range (<10 nm). In contrast, PZ-I and PZ-II caused only slightly shift the size of large colloids toward smaller dimensions while significantly increasing the proportion of large colloids (from 9% to 12% or 13%), thereby disrupting size uniformity. This difference arises from distinct mechanism (shown in Fig. 1e): PZ's strong immobilization effect stabilizes the EDL by effectively fixing cations around iodoplumbate ions, reducing colloidal agglomeration and enhancing size uniformity. In contrast, PZ-I and PZ-II, due to their significant proton dissociation in perovskite solutions, neutralize the charges of iodoplumbate ions and cations[27], destabilizing the EDL and increasing colloidal agglomeration irregularly. This destabilization renders PZ-I and PZ-II unsuitable for producing films with the homogeneous structure required to achieve the high-performance IPSMs.

To validate these findings, 10 cm × 10 cm mini-IPSMs (11 cells in serries, Supplementary Fig. 1a) were fabricated with an FTO/NiO_x/Me-4PACZ/perovskite/C_{60}/BCP/Cu structure (Supplementary Fig. 1b). For IPSMs with an aperture area of 56.5 cm^2, PZ improved module efficiency from 18.2% to 21.5%, while PZ-I and PZ-II either had negligible effects (17.9%) or reduced efficiency (17.0%) (Supplementary Fig. 2 and Supplementary Table 3). These results confirm that PZ is the most effective additive among the three isomers for the scalable fabrication of high-performance IPSMs with homogeneous structural perovskite films.

Properties of homogeneous structural perovskite films

Buliding on the observed effects of PZ on colloidal stability, we investigated its role in perovskite crystallization. As shown in Fig. 2a, scalable preparation of FA-based perovskite films was achieved via a three-step process in air: (1) slot-die coating to form a wet film (Process I), (2) rapid solvent extraction using VASP to obtain a perovskite semi-wet film (Process II), and thermal annealing to complete crystallization (Process III). Top-view scanning electron microscopy (SEM) revealed that PZ significantly increased grain size compared to the control

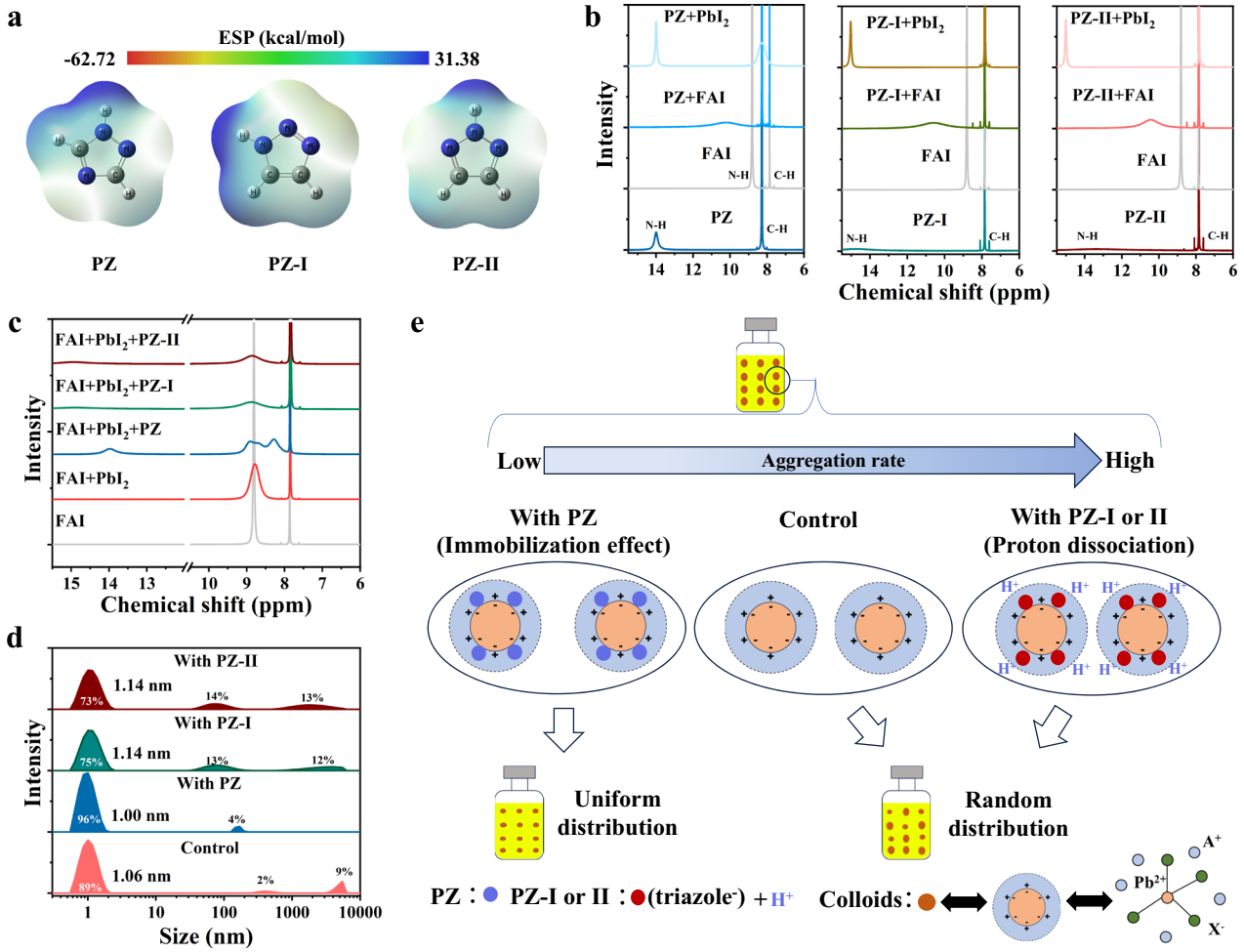

Fig. 1 | Immobilization effect of triazole additives in precursor solutions. **a** Molecular structures and calculated ESP profile of triazole additives. **b** ^{1}H NMR spectra of triazole additives, FAI, triazole additives mixed with FAI, and triazole additives mixed with PbI_2. **c** ^{1}H NMR spectra of FAI and PbI_2, and triazole additives mixed with FAI and PbI_2. **d** DLS analysis of perovskite precursor solutions with triazole additives. **e** Proposed mechanism illustrating the effects of triazole additives on perovskite colloids.

(Supplementary Fig. 3), reducing grain boundaries and improving film quality. The optimal morphology was achieved at a PZ concentration of 1.5 mg mL^{-1}, which was further validated by 1 cm^2 IPSC performance measurements (Supplementary Fig. 4 and Supplementary Table 4).

To evaluate the effect of PZ on film uniformity, we performed photoluminescence (PL) mapping measurements. As shown in Fig. 2b, the PZ-treated film exhibited more uniform PL intensity compared to the control film, demonstrating enhanced film uniformity. Cross-sectional SEM measurements further revealed that PZ benefits the formation of large, monolithic grain arrangement within the perovskite film (Fig. 2c), confirming that PZ enables the preparation of perovskite films with homogeneous structure. This obvious enhancement is primarily attributed to the improved uniformity of colloid size distribution in the precursor solution, as discussed earlier.

The homogeneity of the 10 cm × 10 cm perovskite films was evaluated. As shown in Supplementary Fig. 5, the PZ-treated film possessed a uniform mirror-like black color, while the control film displayed a highly heterogeneous apperance, indicating that PZ effectively enhances the morphology uniformity of large-area perovskite films. To further verify this, the 10 cm × 10 cm perovskite films were divided into 25 equal parts (Fig. 2d) and fabricated into IPSCs. Statistical analysis of the PCE vaules for the 25 solar cells (Fig. 2e and Supplementary Fig. 6) revealed that the PZ-modified cells exhibited a narrower PCE distribution compared to the control cells, demonstrating improved film uniformity. Additionaly, the average PCE of the 25 cells increased from 19.00% to 22.30% with the introduction of PZ, which is attributed to the enhanced performance of the homogeneous structural perovskite films induced by PZ.

To study the effect of the homogeneous structure on the phase uniformity of large-area perovskite films, PL measurements were conducted on five selected regions (marked in black in Fig. 2d). The testing method and device structure are detailed in Supplementary Fig. 7. As shown in Fig. 2f, the control films exhibited strong dispersion in both the position and intensity of PL peaks across the five regions, particularly when tested from the back side, indicating non-uniform film quality and phase distribution. In contrast, the PZ-treated films showed significantly reduced dispersion in PL peak positions and intensities, with notably enhanced PL intensities on the front side. These results strongly proves that PZ not only passivates defects to improve the film quality but also optimizes the phase distribution uniformity of large-area perovskite films[35,36], attributed to the homogeneous structure induced by PZ. As a result, the PZ-modified 10 cm × 10 cm IPSMs achieved a champion PCE of 21.5%, with negligible hysteresis and stable power output (Fig. 2g and Supplementary Fig. 8).

Insights into PZ-induced homogeneous structure in films

The morphology evolution of perovskite films is closely linked to their crystallization process[37,38]. To understand in more detail the effect of PZ on the crystallization process and the formation of homogeneous

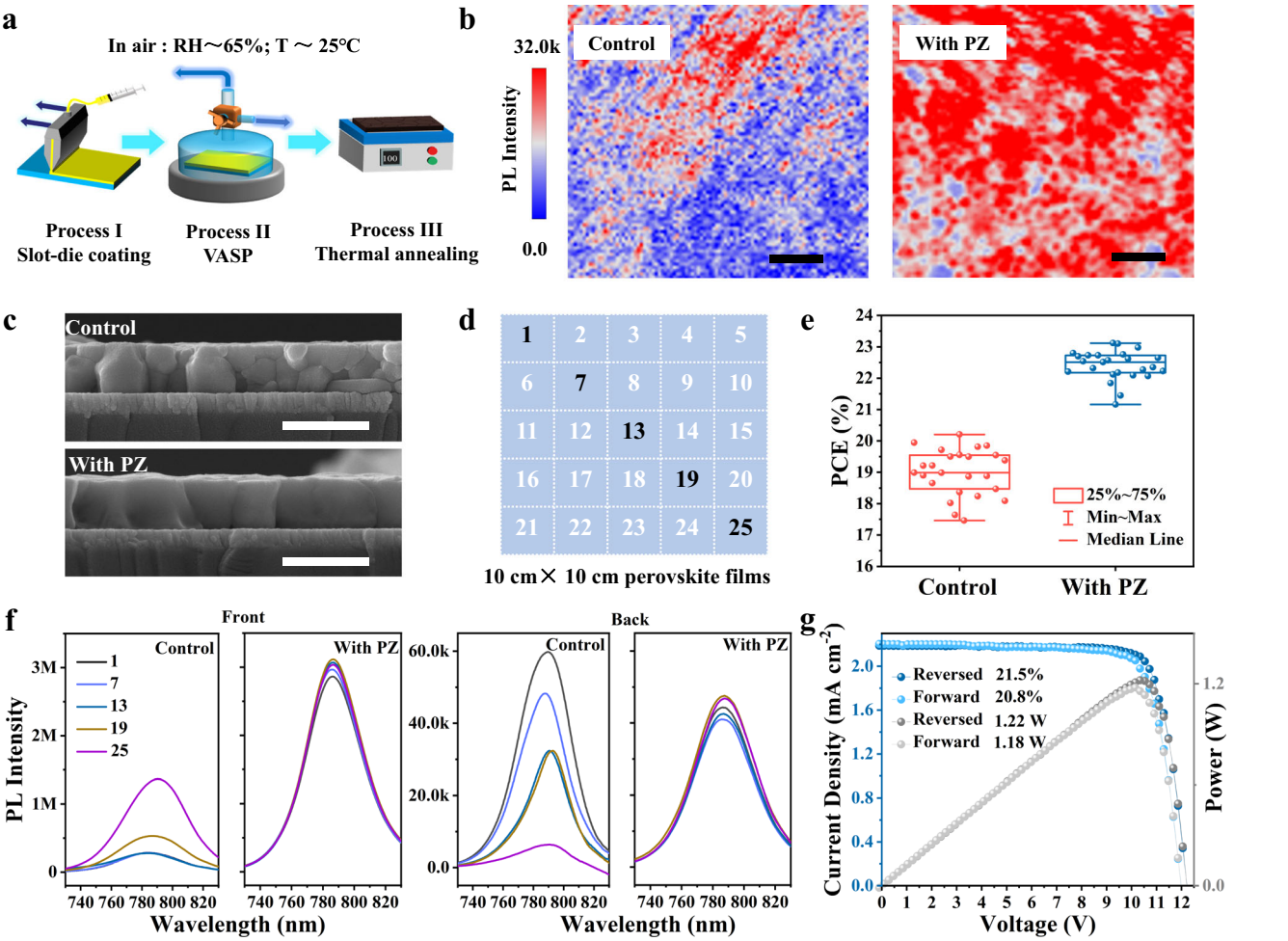

Fig. 2 | Formation of homogeneous structural perovskite films with PZ additive. a Schematic diagram for the large-scale fabrication process of perovskite films. **b** PL mapping images of pervoskite films. Scalebars, 4 μm. **c** Cross-sectional SEM images of pervoskite films. Scalebars, 1 μm. **d** Schematic representation of the 10 cm × 10 cm perovskite films divided into 25 zones. **e** Statistic box plots of the corresponding PCE parameters. Error bars are the standard deviation of PCE over 25 devices. The lines in the middle of the box plots indicate the median values. **f** PL spectra of selected regions from the 10 cm × 10 cm perovskite film. **g** Current density–voltage (*J-V*) and corresponding *P-V* curves of the 10 cm × 10 cm IPSM with PZ (aperture area: 56.5 cm^2).

structure, we performed a series of real-time characterizations to analyze the crystallization kinetics across these process (Fig. 2a). In Process I, the perovskite wet films were in solution state, and their stability is crucial to the subsequent crystallization process[39]. To assess the stability of the perovskite wet films, we monitored their evolution in air using optical microscopy. As shown in Fig. 3a, the stability of wet film with PZ showed a longer window (from 3 to 6 min), which is of great benefit to the precision of the later process. This enhancement in wet film stability by PZ is further confirmed through real-time absorption measurements (Supplementary Fig. 9), primarily attributed to its ability to suppress large-sized colloid agglomeration (Fig. 1d)[5,15].

In Process II, the solvent on the surface of the wet film will be rapidly extracted to form a semi-wet film. To simulate this process, we operated the wet films to high-speed spin-coating (standing for 30 s; spin-coating at 4000 rpm for 45 s; then standing for 30 s) in air. The resulting semi-wet films are shown in Supplementary Fig. 10a. After annealing, it was observed that the film containing PZ showed a black appearance and higher absorption intensity than the control film (Supplementary Fig. 10b). These phenomena not only validate the feasibility of the simulation method, but also demonstrate that PZ can improve the film-forming quality of perovskites. Thus, we monitored this simulation process using real-time PL spectroscopy to understand the role of PZ during Process II. By analyzing the characteristic 760 nm PL peak in real-time results (Fig. 3b and Supplementary Fig. 11), we found that the wet film with PZ exhibited a lower PL intensity during spin-coating, whereas the control film showed a higher intensity. It can be concluded that the perovskite wet film with PZ forms a lower nucleation density during Process II[40]. In Process III, the semi-wet films were annealed to complete of the crystallization process, which was also monitored using real-time PL spectroscopy. By extracting the intensity of the 760 nm PL peak (Fig. 3c and Supplementary Fig. 12), we found that during the initial about 0.7 min of annealing, the PL intensity dropped sharply due to the dissolution of surface nuclei caused by solvent evaporation[41]. Exceeding 0.7 min, the PL intensity was further enhanced until it reaches a stable state, reflecting the transition from surface recrystallization to crystallization completion[40]. Compared to the control sample (11.4 min), the PZ-treated films exhibited a longer crystallization process (12.9 min), which is advantageous for the formation of larger grains.

To further investigate the effect of PZ on the grain arrangement and structural uniformity of perovskite films, we conducted GD-OES measurements to monitor solvent evolution during Process III. For this analysis, dimethyl sulfoxide (DMSO) was used as a replacement for DMPU in the perovskite precursor solvent, with sulfur serving as the tracking element. The feasibility of this substitution was verified by comparing the crystallinity of perovskite films formed in both solvent systems. As shown in Supplementary Fig. 13, the X-ray diffraction

https://doi.org/10.1038/s41467-025-57303-w

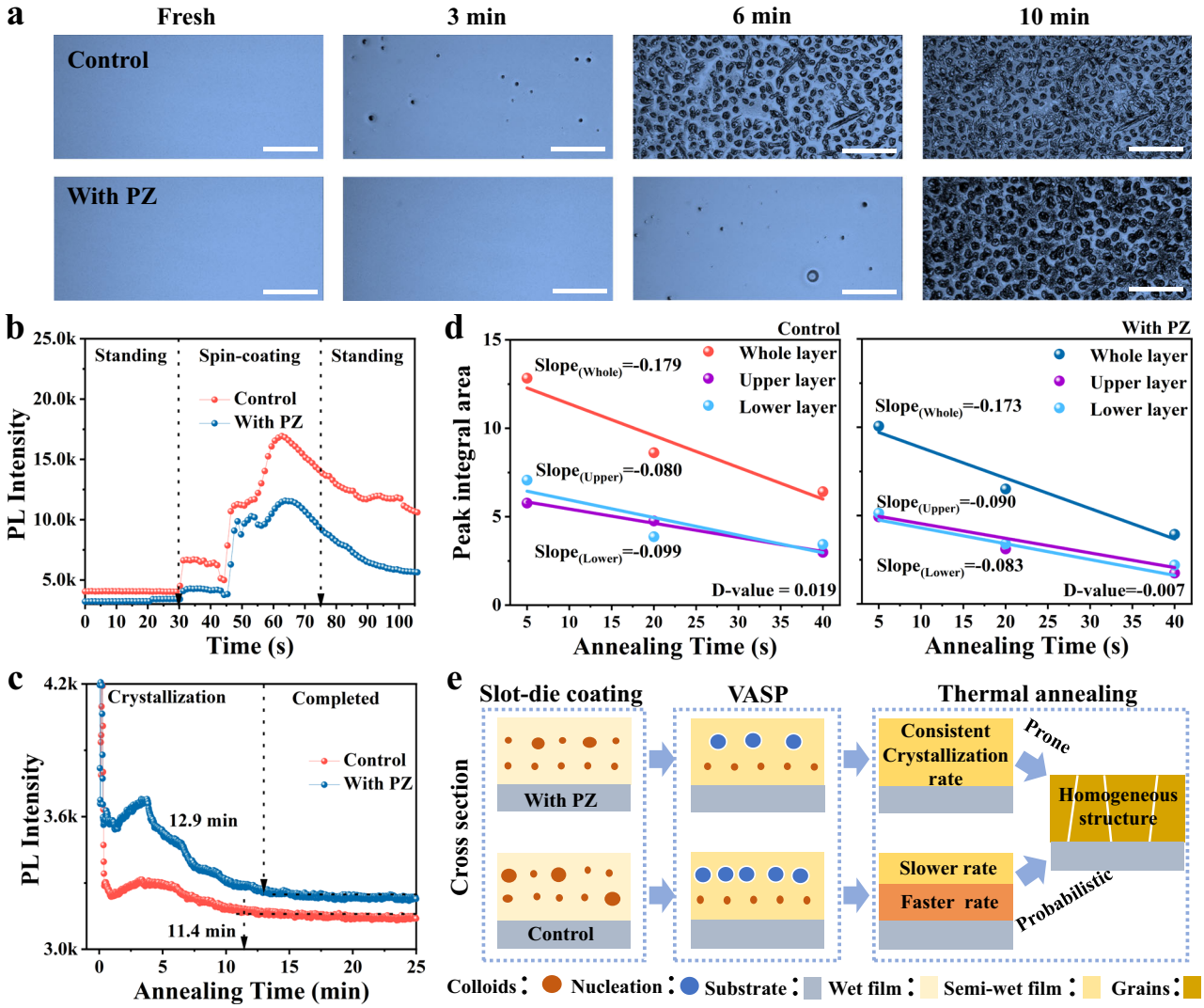

Fig. 3 | Formation mechanism of homogeneous structural perovskite films. **a** Real-time monitoring of perovskite wet films morphology evolutions over time with an optical microscope in air (RH ~ 65%, T ~ 25 °C). Scalebars, 200 μm. **b** Real-time PL intensity at 760 nm of perovskite wet films during high-speed spin-coating in air, simulating the process of VASP. **c** Real-time PL intensity at 760 nm of semi-wet films during annealing in air. **d** Solvent evolution in the upper, lower, and whole layers of control and PZ-treated perovskite precursor films, tracked by GD-OES. **e** Proposed mechanism for scalable perovskite film preparation with homogeneous structure, integrating solvent evolution, crystallization kinetics, and colloidal distribution. The schematic illustrates that when the crystallization rates of the upper and lower layers of the wet films are more consistent, it is prone to form large, monolithic grains. However, even with notable differences in crystallization rates, it is still probabilistic to form such grain structures within a specific range.

(XRD) patterns of the films showed prominent peaks at 14.18° and 28.31°, corresponding to the (001), and (002) crystal planes of cubic-phase FA-based perovskite, consistent with previous reports[42,43]. Obviously, PZ enhanced the crystallinity of perovskite films in both solvent systems, confirming that the solvent substitution had minimal impact on PZ's effects and validating monitoring approach. Compared to the DMSO system, the DMPU solvent system produced films with superior crystallinity, which is why the DMPU system was selected for this study. Importantly, no peak shifts or additional diffraction peaks were observed, confirming that PZ does not integrate into the perovskite lattice. Given its high boiling point (>200 °C), it is inferred that PZ resides at the grain boundaries and film surface after crystallization, where it passivates defects and further improves film quality.

The solvent evalution during Process III was monitored for semi-wet films (Supplementary Fig. 14), revealing two distinct peaks in the GD-OES curves that correspond to the upper and lower layers of the wet film. According to Zheng et al.[25,44], the annealing of FA-based perovskite wet films involve two primary stages: (1) rapid solvent volatilization within 5 s (Stage-1), and (2) subquent crystal growth (Stage-2), which aligns with the trends observed in real-time PL measurements. To evaluate the influence of PZ on the grain arrangement, we integrated the area under the GD-OES curves during the Stage-2 (Fig. 3d). The results showed that PZ reduced the slope of the solvent evolution curve across the whole wet film (from −0.179 to −0.173), indicating that PZ slowed the perovskite crystal growth rate in whole film. Further analysis of the slope difference between the upper and lower layers of the wet film (Supplementary Table 5) revealled that PZ reduced this difference (from 0.019 to 0.007), indicating that PZ promoted a more uniform crystallization rate across the film.

By integrating the crystallization characterization results, and colloidal size distribution data, we propose a mechanism for the PZ-induced formation of perovskite films with homogeneous structure (Fig. 3e). Firstly, PZ strongly immobilized with the compositions in the precursor solution, preventing colloidal agglomeration. This avoids the formation of large colloids with decreased nucleation energy, thus enhancing the stability of the wet film and ensuring a uniform colloidal

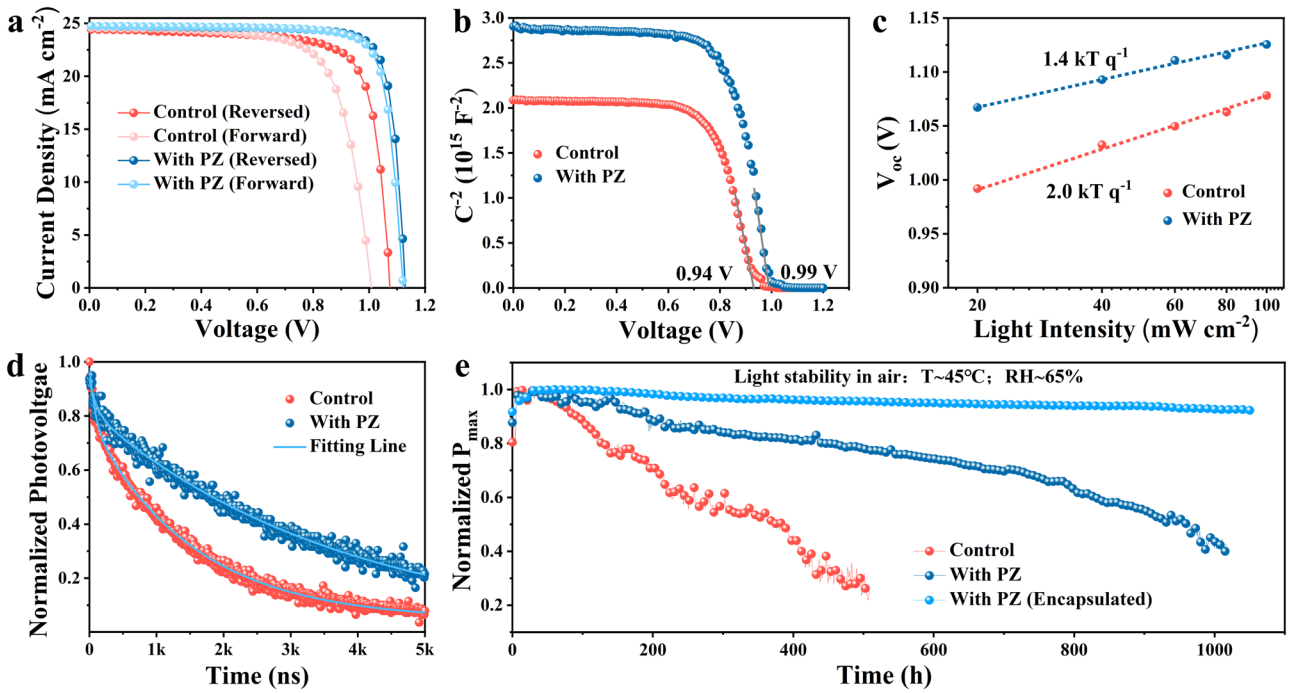

Fig. 4 | Photovoltaic performance. a Champion *J-V* curves of IPSCs with an active area of 1 cm^2. **b** Mott–Schottky plots showing the V_{bi} of IPSCs. **c** Dependence of V_{OC} on light intensity for IPSCs. **d** Transient photovoltage (TPV) decay curves of IPSCs. **e** MPPT of IPSMs under one-sun equivalent white LED illumination in air (T ~ 45 °C, RH ~ 65%).

Table 1 | Photovoltaic parameter summary of IPSCs and IPSMs

Samples	Area (cm^2)	Scanning direction	V_{OC} (V)	J_{SC} (mA cm^{-2})	FF (%)	PCE (%)
Control IPSC	1.0 (Active area)	Reversed	1.07	24.42	77.35	20.21
		Forward	1.02	24.62	73.04	18.40
With PZ IPSC		Reversed	1.13	24.72	82.82	23.13
		Forward	1.12	24.75	81.92	22.70
With PZ IPSM	56.5 (Aperture area)	Reversed	12.21	2.19	80.77	21.5
		Forward	11.99	2.20	78.96	20.8

size distribution. Second, the reduction in large-sized colloids caused by aggregation further decreased the nucleation sites in process II, leading to a lower nucleation density in the semi-wet film. Finally, the reduced nucleation density slowed down the crystal growth process in process III, decreased the overall crystallization rate, and ensures a consistent crystallization rate across the films. This process ultimately produces perovskite films with large, monolithic grain arrangement.

Effect of homogeneous structure on photovoltaic performance

To evaluate the impact of homogeneous structural perovskite films on device performance, we analyzed the photovoltaic characteristics of the optimal IPSCs. The champion *J-V* curves and corresponding performance parameters for IPSCs are depicted in Fig. 4a and Table 1. The PZ-modified device achieved an excellent PCE of 23.13%, with a short-circuit current (J_{SC}) of 24.72 mA cm^{-2}, fill factor (FF) of 82.82% and open-circuit voltage (V_{OC}) of 1.13 V, significantly outperforming the control device (PCE of 20.21%, J_{SC} of 24.42 mA cm^{-2}, FF of 77.35% and V_{OC} of 1.07 V). Notably, the PZ-modified IPSCs exhibited negligible hysteresis. The external quantum efficiency (EQE) spectra (Supplementary Fig. 15) confirmed that the J_{SC} values extracted from the *J-V* curves, further validating the reliability of the measurements. These results indicate that PZ primarily improves V_{OC} and FF, with a similar trend observed in IPSMs (Supplementary Table 3).

To explor the mechanism behind the enhanced device performance, we characterized the defect density and charge carrier dynamics within perovskite films. Space-charge-limited current (SCLC) measurements (Supplementary Figs. 16 and 17) revealed significantly lower trap densities in PZ-treated films (3.3×10^{15} cm^{-3} for hole-only device and 2.5×10^{15} cm^{-3} for electron-only device) compared to control samples (8.3×10^{15} cm^{-3} and 5.8×10^{15} cm^{-3}, respectively). The reduction is attributed to the the homogeneous structure induced by PZ. Time-resolved photoluminescence (TRPL) decay measurements (Supplementary Fig. 18 and Supplementary Table 6) further confirmed this, compared to the control film (τ_{ave} = 138.5 ns), the PZ-treated film displaying an obviously longer carrier lifetime (τ_{ave} = 356.6 ns). These results demonstrate that PZ reduces defect density and enhances charge carrier transport[45]. Then, capacitance-voltage (Mott–Schottky) analysis was conducted to further clarify the impact of homogeneous structure on the built-in potential (V_{bi}) of IPSCs. As shown in Fig. 4b, the V_{bi} of the device with PZ increased from 0.94 V (control) to 0.99 V, which enhances charge separation, transport, and photo-generated carrier collection[44], contributing to the enhanced V_{OC}.

Electrical impedance spectroscopy (EIS) provided additional insights into the influence of PZ on carrier transport and recombination. The device with PZ exhibited a reduced series resistance (R_s) of 3.9 Ω cm^{-2} and an increased recombination resistance (R_{rec}) of 7.1 kΩ cm^{-2}

compared to the control device (R_s = 6.2 Ω cm^{-2}, R_{rec} = 5.5 KΩ cm^{-2}), indicating improved carrier transport and suppressed recombination losses (Supplementary Fig. 19 and Supplementary Table 7). The dependency of V_{OC} on light intensity (Fig. 4c) showed that the ideality factor of the device with PZ decreased from 2.0 (control) to 1.4, approaching the ideal value of 1, which demonstrates effective suppression of trap-assisted charge recombination[46]. Futhermore, the improved V_{OC} decay time from 1452.3 ns to 3699.2 ns also proves that the recombination is strongly inhibited after introducing PZ additive (Fig. 4d and Supplementary Table 8)[47].

To evaluate the impact of homogeneous structural perovskite films on device stability, we first examined the humidity stability of unencapsulated perovskite films. Perovskite films were kept in air at ~65% RH and 25 °C room temperature. As depicted in Supplementary Fig. 20a, the control film bleached completely after 30 days, whereas the PZ-treated film maintained its black color, demonstrating significantly improved resistance to degradation. XRD analysis (Supplementary Fig. 20b) confirmed that PZ suppressed phase transitions and perovskite decomposition, attributed to hydrogen bonding between PZ and FAI[34], and improved film quality. As a result, IPSCs with PZ retained over 90% of their initial PCE after 30 days of air storage (Supplementary Fig. 20c).

The light stability of IPSMs was further evaluated using maximum power point tracking (MPPT) under one-sun equivalent white-light LED illumination in air atmosphere (T ~ 45 °C; RH ~ 65%). As shown in Fig. 4e, the unencapsulated IPSM with PZ maintained ~80% of its inital PCE even after 460 h, while the control IPSM decayed to a similar level within only 120 h. This remarkable improvement in light stability is mainly due to the enhanced film quality induced by PZ. To access the practical application potential of PZ-modified IPSMs, we encapsulated the modules and conducted PCE certification at the National Institute of Measurement and Testing Technology. Encouragingly, the encapsulated IPSM with PZ achieved an excellent certified PCE of 20.3% and a P_{max} of 1.15 W (Supplementary Fig. 21). Furthermore, the encapsulated IPSM maintained 94% of its inital efficiency after 1000 h of air aging, demonstrating a good work stability (Fig. 4e). Finally, we successfully powered a 1W-rated fan under outdoor sunlight (Supplementary Movie 1), showcasing a great potential for practical outdoor applications.

Discussion

In this work, we systematically designed and investigated the immobilization effect of the PZ additive, providing a comprehensive analysis of its influence on precursor colloidal distribution, nucleation, and crystallization processes. Through real-time characterization techniques, we directly verified that the immobilization effect of PZ facilitates the formation of large, monolithic grains, enabling the formation of homogeneous 10 cm × 10 cm FA-based perovskite films in air. As a result, slot-die coated IPSCs and IPSMs achieved satisfying PCEs of 23.13% (active area of 1.0 cm^2) and 21.5% (certified 20.3%; aperture area of 56.5 cm^2), ranking among the highest reported efficiencies for IPSMs with an active area > 50 cm^2. Furthermore, the working stability of IPSMs was significantly enhanced. This study provides a promising strategy for the industrial-scale production of large-area IPSMs, as well as an effective guidance for large-scale commercialization of PSCs.

Methods

Materials

N, N-dimethylformamide (DMF), DMPU, 1H-1, 2, 4-triazole (PZ, 99%), 1H-1, 2, 3-triazole (PZ-I, 98%), and 2H-1, 2, 4-triazole (PZ-II, 98%), and C_{60} were purchased from Sigma-Aldrich. Lead (II) iodide (PbI_2, 99.99%), Formamidinium iodide (FAI), methylammonium bromide (MABr), Methylamine hydrochloride (MACl, 99%), Cesium iodide (CsI), bathocuproine (BCP, >99%) and [4-(3,6-dimethyl-9H-carbazol-9-yl)butyl] phosphonic acid (Me-4PACz) were purchased from Xi'an Polymer Light Technology Corp.

Perovskite precursor solutions

We prepared the $Cs_{0.05}(MA_{0.05}FA_{0.95})_{0.95}Pb(I_{0.95}Br_{0.05})_3$ triple-cation precursor solution (1.0 M) by dissolving 12 mg CsI, 155.3 mg FAI, 35.7 mg $MAPbBr_3$, 470 mg PbI_2, and 10 mg MACl in 1 mL mixed solvent of DMF and DMPU (DMF: DMPU = 9:1, vol%). The PZ was added into perovskite precursor solution with different contents (from 0 to 2 mg mL^{-1} with a 0.5 mg mL^{-1} step). When preparing the perovskite precursor solutions for PZ-I and PZ-II, the concentration of both additives was optimized to 1.5 mg mL^{-1}.

Device fabrication

FTO/glass substrates (10 cm × 10 cm) were cleaned by ultra-sonication in isopropanol, acetone and water for 20 min, respectively. Then, the substrates were dried by nitrogen flow and treated by an ultraviolet for 10 min. NiO_x layer (40 nm) was grown by RF sputtering on washed FTO substrates at room temperature with a chamber pressure of 0.37 Pa, RF power of 200 W, argon flow rate of 100 sccm for 40 min. The sputtered NiO_x film was annealed at 300 °C for 30 min under ambient conditions. To passivate the defects at the interface between the perovskite film and NiO_x, we deposited Me-4PACZ film on the NiO_x film surface by blade coating in air[47]. The concentration of Me-4PACZ in isopropanol is 0.5 mg mL^{-1}, the scraping gap is 0.15 mm, and the speed is 60 mm s^{-1}. After that, the prepared perovskite precursor solution with different concentrations of additives were deposited in air by slot-die coating technology with a feed pump speed of 2 μL s^{-1}, a gap (between the slip and substrate) of 0.25 mm, and a substrate moving speed of 10 mm s^{-1}. Then, the wet films obtained from the slot-die coating were quickly transferred to a vacuum container (placed in a vacuum of 2 Pa for 30 s) for rapid solvent evaporation to obtain semi-wet films. After that, the semi-wet films were heated at 100 °C for 30 min on a hotplate in air to obtain dark perovskite films. After cooling down, 10 cm × 10 cm films were evenly divided into 25 piecesa by a slicer, with each piece measuring 2 cm × 2 cm in size. After that, C_{60} (20 nm), and BCP (7 nm) in sequential order were thermally evaporated on the surface of the cut film in a vacuum chamber (<5 × 10^{-4} Pa). Finally, the Cu film (~100 nm) was thermally evaporated as a counter electrode by a shadow mask to define an active area of 1.0 cm^2. The preparation of IPSMs and IPSCs is basically same except for cutting the 10 cm × 10 cm films into 25 parts. It is worth noting that P1, P2, and P3 scribing was used to fabricate series-connected modules, where P1 and P3 were divided the module into sub-cells, and P2 connected the sub-cells. Fristly, the red laser of 1064 nm was used to scribe the 10 cm × 10 cm FTO substrate to form 11 strips (P1). The NiO_x layer, Me-4PACZ layer, perovskite film, C_{60} (50 nm) film, and BCP layer (7 nm) were prepared by the same method as listed above. After that, the obtained perovskite/C_{60}/BCP films were etched by a green laser of 532 nm (P2), and performed electrode edge cleaning (with a width of 9 mm on both sides). Finally, the Cu film (~100 nm) was thermally evaporated as a counter electrode, divided by green laser (P3) and performed edge cleaning again (8 mm wide on each other side) for device packaging. The aperture area was determined using a mask with a defined area of 56.5 cm^2, as shown in Supplementary Fig. 1a.

Module encapsulation process

EVA film is placed on both the metal electrode and glass side, and then treated with thermal softening. The heating temperature is set to 90 °C, and the thermal pressing time is set to 15 min, which includes vacuum for 1 min, bonding time for 4 min, and de-bubbling for 10 min.

Characterization

DLS measurements were performed by a MALVERN-Zetasizer Nano S90 system. NMR spectroscopy for precursor was performed by using a Bruker-Avance III HD 400 MHz spectrometer. PL, PL mapping, and TRPL spectra of the samples were measured using a Fluorolog-3 fluorescence spectrophotometer. A 510 nm laser with a full width at half maximum of 1.5 nm was employed as the excitation light source.

The PL decay curves were fitted using a double-exponential decay model. All experimental details and data fitting procedures related to the PL measurements are discussed in detail in the Supplementary Information. SEM was conducted by a field-emission SEM (FEI-Inspect F50, Holland). Real-time UV–vis absorption and real-time PL spectra were recorded by a dynamic spectrometer (DU200). UV–vis absorption spectra were measured by an ultraviolet-visible (UV–vis) spectrophotometer (Shimadzu, UV-3101 PC). XRD measurements were carried out using a Bede D1 system with Cu Kα radiation. GD-OES analyses were performed using a HORIBA Jobin Yvon GD Profiler 2 with Quantum Software. The instrument configuration included a RF-generator (at 13.56 MHz), a standard HORIBA Jobin Yvon glow discharge source with a cylindrical anode of 4 mm internal diameter and two optical spectrometers (a polychromator and a monochromator) for fast-optical detection. No loss in time resolution was ensured thanks to the detection system, composed of independent photomultiplicators (PM), which guarantee simultaneous detection of the signals corresponding to multiple wavelengths with spectral resolution of 12 pm. The emission signals of 47 elements were recorded but only the signals of the species of interest are discussed in the paper. The selected wavelength for Pb and S were 220.357 and 180.738 nm, respectively. The *J-V* curves the solar cells and modules were measured in air using a Keithley 2400 Source Meter under standard AM 1.5 G solar irradiation (100 mW cm^{-2}). The *J-V* characteristics of all the devices were recorded over voltage ranges of 1.2 V to −0.1 V and 13 V to −0.1 V, respectively, with 50 and 70 sweep points, and dwell times of 30 ms and 10 ms, respectively. For the SCLC test, the voltage scan range was 0 V to 3 V, with 90 sweep Points and a dwell time of 30 ms. The EQE spectra of the IPSCs were measured by a QTest Station 500TI system (Crowntech. Inc., USA), where the monochromatic light intensity was calibrated using a reference silicon detector. The dark capacitance curve was measured by Agilent 4294 A under dark conditions, with varying DC biases with an AC frequency range of 10 Hz to 0.1 MHz. MPPT (ZN-SCT-SYSTEM) of the modules was measured in air under one-sun equivalent white LED illumination (T: ~ 45 °C, RH: ~ 65%).

Simulation methods

The ESP and interaction energy of intermolecular are calculated by Gauss 09 based on density functional theory. All the molecules were optimized and converged, and no obvious imaginary frequencies appeared. The calculation method is B3LYP and all electron double-ξ valence basis sets of 6-311 + G (d, p).

Reporting summary

Further information on research design is available in the Nature Portfolio Reporting Summary linked to this article.

Data availability

All relevant data are presented in the Supplementary Information/Source Data file (Figshare https://doi.org/10.6084/m9.figshare.26509918). Source data are provided with this paper.

References

1. Zhang, Z. et al. Suppressing ion migration by synergistic engineering of anion and cation towards high-performance inverted perovskite solar cells and modules. *Adv. Mater.* **24**, 2313860 (2024).
2. Uddin, M. A. et al. Iodide manipulation using zinc additives for efficient perovskite solar minimodules. *Nat. Commun.* **15**, 1355 (2024).
3. Rong, Y. et al. Toward industrial-scale production of perovskite solar cells: screen printing, slot-die coating, and emerging techniques. *Phys. Chem. Lett.* **9**, 2707–2713 (2018).
4. Cheng, Y. et al. Progress in air-processed perovskite solar cells: from crystallization to photovoltaic performance. *Mater. Horiz.* **6**, 1611–1624 (2019).
5. Yang, Z. et al. Slot-die coating large-area formamidinium-cesium perovskite film for efficient and stable parallel solar module. *Sci. Adv.* **7**, 3749 (2021).
6. Cheng, Y. et al. The detrimental effect of excess mobile ions in planar $CH_3NH_3PbI_3$ perovskite solar cells. *J. Mater. Chem. A* **4**, 12748–12755 (2016).
7. Tiep, N. H. et al. Recent advances in improving the stability of perovskite solar cells. *Adv. Energy Mater.* **6**, 1501420 (2016).
8. Wang, F. et al. Steering the crystallization of perovskites for high-performance solar cells in ambient air. *J. Mater. Chem. A* **7**, 12166–12175 (2019).
9. Bella, F. et al. Improving efficiency and stability of perovskite solar cells with photocurable fluoropolymers. *Science* **354**, 203–206 (2016).
10. Gao, H. et al. Improving efficiency and stability of perovskite solar cells with photocurable fluoropolymers. *ACS Appl. Mater. Interfaces* **17**, 9110–9117 (2015).
11. Lee, J. et al. Achieving large-area planar perovskite solar cells by introducing an interfacial compatibilizer. *Adv. Mater.* **29**, 1606363 (2017).
12. Bu, T. et al. Lead halide-templated crystallization of methylamine-free perovskite for efficient photovoltaic modules. *Science* **372**, 1327–1332 (2021).
13. Chen, S. et al. Stabilizing perovskite-substrate interfaces for high-performance perovskite modules. *Science* **372**, 902 (2021).
14. Lee, D.-K. et al. Scalable perovskite coating via anti-solvent-free lewis acid–base adduct engineering for efficient perovskite solar modules. *J. Mater. Chem. A* **9**, 3018–3028 (2021).
15. Liu, C. et al. Understanding of perovskite crystal growth and film formation in scalable deposition processes. *Chem. Soc. Rev.* **49**, 1653–1687 (2020).
16. Xiao, M. et al. A fast deposition-crystallization procedure for highly efficient lead iodide perovskite thin-film solar cells. *Angew. Chem. Int. Ed.* **53**, 9898–9903 (2014).
17. Son, D. Y. et al. Self-formed grain boundary healing layer for highly efficient $CH_3NH_3PbI_3$ perovskite solar cells. *Nat. Energy* **1**, 16081 (2016).
18. Zhou, Y. et al. A fast deposition-crystallization procedure for highly efficient lead iodide perovskite thin-film solar cells. *J. Mater. Chem. A* **3**, 8178–8184 (2015).
19. Huang, F. et al. Gas-assisted preparation of lead iodide perovskite films consisting of a monolayer of single crystalline grains for high efficiency planar solar cells. *Nano Energy* **10**, 10–18 (2014).
20. Li, X. et al. A vacuum flash-assisted solution process for high-efficiency large-area perovskite solar cells. *Science* **353**, 58–62 (2016).
21. Lin, Y. et al. π-Conjugated lewis base: efficient trap-passivation and charge-extraction for hybrid perovskite solar cells. *Adv. Mater.* **29**, 1604545 (2017).
22. Ahn, N. et al. Highly reproducible perovskite solar cells with average efficiency of 18.3% and best efficiency of 19.7% fabricated via lewis base adduct of lead(II) iodide. *J. Am. Chem. Soc.* **137**, 8696–8699 (2015).
23. Xie, L. et al. Importance of functional groups in cross-linking methoxysilane additives for high-efficiency and stable perovskite solar cells. *ACS Energy Lett.* **4**, 2192–2200 (2019).
24. Noel, N. K. et al. Importance of functional groups in cross-linking methoxysilane additives for high-efficiency and stable perovskite solar cells. *ACS Nano* **8**, 9815–9821 (2014).
25. Zheng, D. et al. Control of perovskite film crystallization and growth direction to target homogeneous monolithic structures. *Nat. Commun.* **13**, 6655 (2022).
26. Lobo, L. et al. Depth profile analysis with glow discharge spectrometry. *J. Anal. Spectrom.* **32**, 920–930 (2017).

27. Amoroso, D. et al. The central role of colloids to explain the crystallization dynamics of halide perovskites: A critical review. *Matter* **7**, 2399–2430 (2024).
28. Li, B. et al. Colloidal engineering for monolayer $CH_3NH_3PbI_3$ films toward high performance perovskite solar cells. *J. Mater. Chem. A* **5**, 24168–24177 (2017).
29. Flatken, M. A. et al. Role of the alkali metal cation in the early stages of crystallization of halide perovskites. *Chem. Mater.* **34**, 1121–1131 (2022).
30. Guan, Q. et al. Triazoles in medicinal chemistry: physicochemical properties, bioisosterism, and application. *J. Med. Chem.* **67**, 7788–7824 (2024).
31. Jiang, H. et al. A design strategy of additive molecule for PSCs: anchoring intrinsic properties of functional groups by suppressing long-range conjugation effect. *Chem. Eng. J.* **427**, 131676 (2022).
32. Zhu, T. et al. The stabilization of formamidinium lead tri-iodide perovskite through a methylammonium-based additive for high-efficiency solar cells. *Sol. RRL* **4**, 2000348 (2020).
33. Zheng, D. et al. What are methylammonium and solvent fates upon halide perovskite thin film preparation and thermal aging? *Adv. Mater. Interfaces* **9**, 2201436 (2022).
34. Li, M. et al. Orientated crystallization of FA-based perovskite via hydrogen-bonded polymer network for efficient and stable solar cells. *Nat. Commun.* **14**, 573 (2023).
35. Yuan, S. et al. Simultaneous cesium and acetate coalloying improves efficiency and stability of $FA_{0.85}MA_{0.15}PbI_3$ perovskite solar cell with an efficiency of 21.95%. *Sol. RRL* **3**, 1900220 (2019).
36. Yuan, S. et al. NbF_5: a novel α-phase stabilizer for FA-based perovskite solar cells with high efficiency. *Adv. Funct. Mater.* **29**, 1807850 (2019).
37. Troughton, J. et al. Humidity resistant fabrication of $CH_3NH_3PbI_3$ perovskite solar cells and modules. *Nano Energy* **39**, 60–68 (2017).
38. Zeng, L. et al. Humidity resistant fabrication of $CH_3NH_3PbI_3$ perovskite solar cells and modules. *Energy Environ. Sci.* **13**, 4666–4690 (2020).
39. Yang, M. et al. Perovskite ink with wide processing window for scalable high-efficiency solar cells. *Nat. Energy* **2**, 17038 (2017).
40. Yang, T. et al. Amidino-based Dion-Jacobson 2D perovskite for efficient and stable 2D/3D heterostructure perovskite solar cells. *Joule* **7**, 574–586 (2023).
41. Yan, Y. et al. Implementing an intermittent spin-coating strategy to enable bottom-up crystallization in layered halide perovskites. *Nat. Commun.* **12**, 6603 (2021).
42. Liu, Y. et al. 20-mm-large single-crystalline formamidinium-perovskite wafer for mass production of integrated photodetectors. *Adv. Opt. Mater.* **4**, 1829–1837 (2016).
43. Yuan, S. et al. Dual-functional passivators for highly efficient and hydrophobic FA-based perovskite solar cells. *Chem. Eng. J.* **433**, 133227 (2022).
44. Zheng, D. et al. Control of the quality and homogeneity of halide perovskites by mixed-chloride additives upon the film formation process. *J. Mater. Chem. A* **9**, 17801–17811 (2021).
45. Cai, Y. et al. Multifunctional enhancement for highly stable and efficient perovskite solar cells. *Adv. Funct. Mater.* **31**, 2005776 (2021).
46. Kuik, M. et al. Trap-assisted recombination in disordered organic semiconductors. *Phys. Rev. Lett.* **107**, 256805 (2011).
47. Al-Ashouri, A. et al. Monolithic perovskite/silicon tandem solar cell with >29% efficiency by enhanced hole extraction. *Science* **370**, 1300–1309 (2020).

Acknowledgements

This work is financially supported by the National Natural Science Foundation of China (62104028 T.Z., 62174021 S. L., and 62104219, P.Z.), Creative Research Groups of the National Natural Science Foundation of Sichuan Province (2023NSFSC1973, S.L.), Basic and Applied Basic Research of Guangzhou Science and Technology Planning Project (2023A04J1726, Y.W.), Municipal University-Enterprise Joint Funding of Guangzhou Science and Technology Plan Project (2023A03J0124, Y.W.), Sichuan Science and Technology program (MZGC20230008, H.Z.), Fundamental Research Funds for the Provincial Universities of Zhejiang (2023YW04, P.Z.), Natural Science Foundation of Sichuan Province (2022NSFSC0899, T.Z.), China Postdoctoral Science Foundation (2021M700689, T.Z.), Sichuan Province Key Laboratory of Display Science and Technology, and Natural Science Foundation of Zhejiang Province (LY22F040002, P.Z.).

Author contributions

S.Y., S.L., and T.Z. supervised the project and co-wrote the manuscript. S.Y. and S.L. conceived the idea and designed the experiments. S.Y. conducted the majority of the experiments. D.Z. primarily carried out the GD-OES characterizations, analyzed the corresponding data, and contributed to the mechanistic understanding. Y.W. and Z.D. performed the real-time experiments, and assisted with real-time date analysis. F.Q, L.W., X.L., H.Z., and P.Z. contributed to film and device characterizations. D.Z., T.Z., and T.P. provided valuable suggestions for the manuscript. T.P. further refined the grammar and language of the article. All authors discussed the results and contributed to the manuscript revisions.

Competing interests

The authors declare no competing interests.

Additional information

Supplementary information The online version contains supplementary material available at https://doi.org/10.1038/s41467-025-57303-w.

Correspondence and requests for materials should be addressed to Ting Zhang or Shibin Li.

Peer review information *Nature Communications* thanks Rui Wang, Shuai You and the other anonymous reviewer(s) for their contribution to the peer review of this work. A peer review file is available.